UCRL-ID-151383

Optics, Diagnostics and Applications for Fourth-Generation Light Sources

A. Wootton, et al

February 5, 2003

U.S. Department of Energy
Lawrence Livermore National Laboratory

DISCLAIMER

This work was performed under the auspices of the U. S. Department of Energy by the University of California, Lawrence Livermore National Laboratory under Contract No. W-7405-Eng-48.

Optics, diagnostics and applications for fourth-generation light sources

Wootton, A., T. Barbee, R. Bionta, H. Chapman, T. Ditmire, G. Dyer, J. Kuba, A. Jankowski, R. London, D. Ryutov, R. Shepherd, V. Shlyaptsev, A. Toor

Lawrence Livermore National Laboratory, 7000 East Ave, Livermore, CA 94550, USA

Abstract

The Linac Coherent Light Source (LCLS) is a 1.5 to 15 Å-wavelength free-electron laser (FEL), proposed for the Stanford Linear Accelerator Centre (SLAC). The photon output consists of high brightness, transversely coherent pulses with duration < 300 fs, together with a broad spontaneous spectrum with total power comparable to the coherent output. The output fluence, and pulse duration, pose special challenges for optical component and diagnostic designs. We first discuss the specific requirements for the initial scientific experiments, and our proposed solutions. We then describe the supporting research and development program that includes: 1) radiation field modelling, 2) experimental and theoretical material damage studies, 3) high resolution, high fluence-tolerant optical design, fabrication, and testing, (including material manufacturing), and 4) diagnostic design and testing.

PACS: 41.50.+h Keywords: x-ray optics, x-ray diagnostics, x-ray damage, LCLS.

1. Introduction

The DOE Office of Basic Energy Science (OBES) has endorsed research and development (R&D) towards a fourth-generation light source [1] based on a LINAC-driven x-ray free electron laser (XFEL) [2]. The Linac Coherent Light Source (LCLS) [3,4], directed by Dr. J Galayda, is now being built at SLAC: Critical Decision 0, a statement of mission need, was signed on 13 June 2001, and on October 16, 2002, DOE approved the Preliminary Project Baseline Range (CD-1) for the LCLS.

Such an XFEL would operate in an entirely new physics regime, self-amplified spontaneous emission (SASE), made possible by demonstrated advances in producing low-emittance electron beams (for a list of SASE-related experimental results, see http://www-ssrl.slac.stanford.edu/lcls/). The unprecedented brightness of such a source, and the short pulse length, highlight demanding requirements as well as innovative design opportunities for the optical and diagnostics systems. The normal fluence (J. cm^{-2}) at the undulator exit far exceeds those required to melt most materials. The challenge is somewhat alleviated downstream, where the natural divergence of the beam (1 μrad at 8 keV, 10 μrad at 1 keV) reduces the fluence.

Lawrence Livermore National Laboratory is responsible for the x-ray optics and diagnostics of the LCLS, under the current project management of Dr. R. Bionta. The R&D described in this document represents the output of a three-year Laboratory

Directed R&D program initiated by Dr. A. Toor (LLNL, retired). The purpose of the project was:

a) to define the generic requirements for optical and diagnostic components, based on a set of first experiments,

b) to model the radiation field,

c) to research both experimentally and theoretically the interaction of the radiation field with matter, and hence to define operational limits for optics and diagnostic based on damage,

d) to develop optical components for beam manipulation and generic experiments,

e) to develop diagnostics for characterizing beam performance,

f) Progress made in each of these areas is now described.

2. The requirements

The requirements for x-ray optics and diagnostics that will allow the first experiments to be initiated on the LCLS are deduced from the book "LCLS, the first experiments", September 2000 [5], and discussions with various task force members. In translating the User and facility requirements to hardware, the attributes of the FEL x-ray output must be considered. Detailed properties of both the coherent and spontaneous radiation have been calculated. The characteristics that are most relevant for the beam transport and optics design (including power density on the optical elements) are shown in Table 2.1 for locations approximating two experimental Halls, A and B (see below).

Table 2.1 Characteristics of the FEL x-ray beam

FEL photon energy	**0.828 keV (4.54 GeV electrons)**		**8.27 keV (14.35 GeV electrons)**	
	FEL fundamental	Spontaneous	FEL fundamental	Spontaneous
Energy per pulse (mJ)	3	1.4	2.5	22
Peak power (GW)	11	4.9	9	81
Photons/pulse	23×10^{12}		1.9×10^{12}	
Divergence (fwhm, mrad)	9	780	1	250
Spot (fwhm) at 50 m Hall A (mm)	610	Limited by apertures	130	Limited by apertures
Spot (fwhm) at 400 m Hall B (mm)	4400		570	
Peak energy density at 50 m Hall A (J. cm^{-2})	0.59		11.9	
Peak energy density at 400 m Hall B (J. cm^{-2})	0.01		0.57	

Two experimental halls are planned, shown in Figures 2.1 (an overall plan), 2.2 and 2.3. One is close to the undulator exit (Hall A, starting about 50 m from the undulator end) and one is considerably farther downstream (Hall B, starting about 400 m from the undulator end). The total experimental floor area will allow the installation of several experimental stations; the hall locations are determined by local access roads and topography. Optics in Hall B will experience a reduced power density that should allow a wide range of materials to be used for samples and optical elements. Hall A will be useful for those experiments requiring maximum power density.

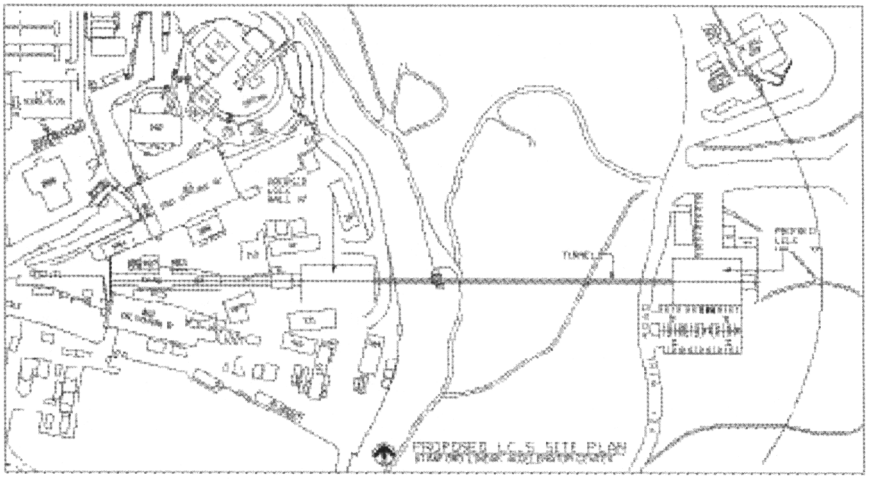

Figure 2.1 LCLS site plan showing experimental halls.

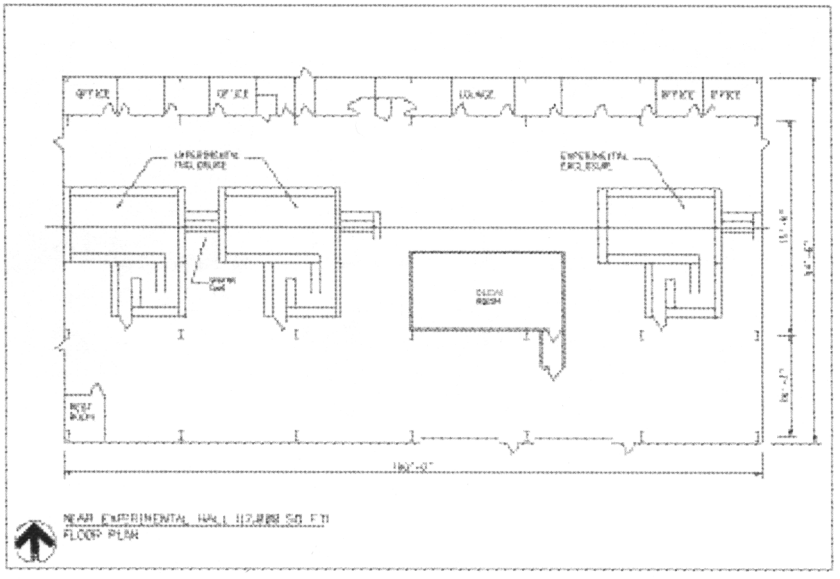

Figure 2.2 Layout of Experimental Hall A

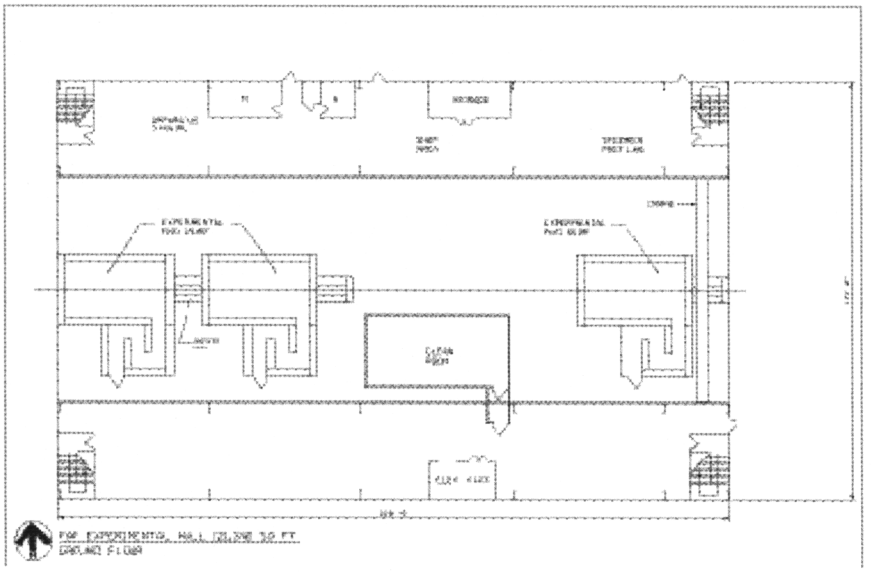

Figure 2.3 Experimental Hall B

An additional reason for a near hall (Hall A) involves the transmission of the spontaneous synchrotron radiation (SR) to experiments. Close to the undulator, a few-mm aperture should transmit a usable fraction of this spectrum. Transporting the same SR cone to the far hall would require an unworkably-large vacuum aperture.

2.1 Optics requirements

Within the two experimental halls A and B are a series of enclosures and hutches. Based on the first experiments document, these will perform the following functions, or house the following equipment:

Front End Enclosure: Fixed masks, a fast valve, vertical and horizontal slits (2 of each), a gas attenuator, a variable-thickness solid attenuator, and a beam stop including a burn-through monitor.

Hutch A1: The first hutch in Hall A will contain optical elements that condition the x-ray beam for the Hall A experiments: Dual-mirror harmonic rejection system, spools, chambers, and beam stop.

Hutch A2: This will house LCLS experiments. It will also contain beam-conditioning optics that need to be close to the experiments, in particular, focusing systems with short focal length: Kirkpatrick-Baez focusing system, refractive focusing system, apertures, attenuator, beam intensity monitors, sample chamber, beam stop.

Hutch A4: This will initially be used for commissioning diagnostics: Diagnostics tank, fixed mask and beam stop, an insertable beam stop with integral burn-through detector.

Inter hall transport: A beam pipe connects the two main halls through a tunnel. It is about 250 m long. Access will be available along the length of the tunnel. In the center of the tunnel, a diagnostics tank will permit beam intensity and position measurements.

Hutch B1: The first hutch in Hall B will contain optical elements which condition the x-ray beam for the Hall B experiments. Only one such element will be included in the initial LCLS, though space is made available for future optics. Hall B is intended primarily for experiments which prefer to be far from the source, in order to reduce the peak intensity or to allow focusing to a minimum spot size: Monochromator, spools, chambers, and beam stop, diagnostics chamber for diagnostics associated with adjustment of the monochromator. It also contains several spool pieces that may in the future be replaced by additional mirror systems and monochromators. At the back end of Hutch B1 is an insertable beam stop with integral burn-through detector.

Hutch B2: This will house LCLS experiments. It will also contain beam-conditioning optics that need to be close to the experiments, in particular, focusing systems with short focal length: pulse split/delay, focusing system, apertures, attenuator, beam intensity monitors, sample chamber, beam stop, insertable beam stop with integral burn-through detector.

Hutch B4: This will initially be used for facility diagnostics: diagnostics tank, beam stop.

2.2. Diagnostics requirements

The diagnostics are located in "diagnostics tanks" distributed along the beam line as shown in Figure 2.4. The diagnostics fall into two categories: 1) Facility/Monitoring diagnostics, and 2) Commissioning diagnostics.

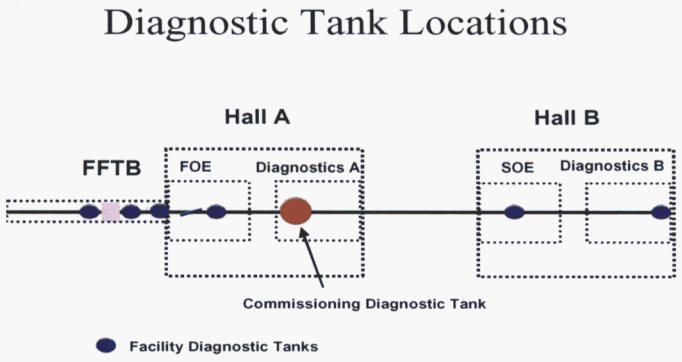

Figure 2.4 Tank locations for LCLS x-ray diagnostics

The facility diagnostics mainly provide pulse-to-pulse information on the beam energy, spatial shape, and centroid, as it exits the undulator and is modified and transported through the beam transport systems to the experimental halls. Because of the fluctuating nature of the SASE FEL it is critical to monitor these beam parameters on a pulse-by-pulse basis. This information is used to 1) provide feedback on the FEL performance, 2) aid in adjusting, monitoring, and setting facility optical systems (slits, attenuators, monochromator) and 3) provide energy shape and centroid information to users. These diagnostics are located after the slits and attenuators in the Front End Enclosure, after the mirrors in the upstream end of Hall A, after the monochromator in the upstream and of Hall B, and at the very end of Hall B. They are intended to be "non-intrusive" if possible, allowing most of the beam to pass through without substantial modification. Avoiding some type of modification (coherence, intensity, etc.) may be difficult, especially at the lowest FEL photon energy.

The commissioning diagnostics are intended to measure the basic FEL performance parameters during commissioning and may be "intrusive". The goals of the commissioning diagnostics are to measure:

a) Total pulse energy
b) Pulse Length
c) Photon Energy Spectrum
d) Transverse coherence
e) Spatial Shape and Centroid location
f) Divergence

Table 2.2 A summary of optical components

Campaign	E (keV)	Challenging requirements	Fluence ($J.cm^{-2}$)
Atomic physics	~ 1	remove SR and third harmonic, focus to < 0.1 μm	0.54
Plasma physics	~ 8	beam focus to < 10 μm, synchronize to a short pulse laser	8.45
Nanoscale dynamics	up to 24	beam split with inter-beam delays from 10^{-12} to 10^{3} s	0.614 at 8 keV
Biology	0.8 to 8	beam temporal compression or time slicing, and focusing, to 10^{8} photons/A^2; synchronization to target.	0.01 to 0.54
Diagnostics	0.8 to 24	pulse temporal history, synchronization, coherence	0.008 to 0.51

The pulse energy, pulse length, spectrum and transverse coherence measurements will be performed in the "Commissioning Diagnostics Tank" in Hutch A4. The divergence

and shape measurements will be made by the "facility diagnostics" distributed along the beam line.

Based on the description of the first experiments, a summary of optical component challenges (photon energy, focusing, fluence etc.) has been derived, and is found in Table 2.2

3. Radiation field modeling

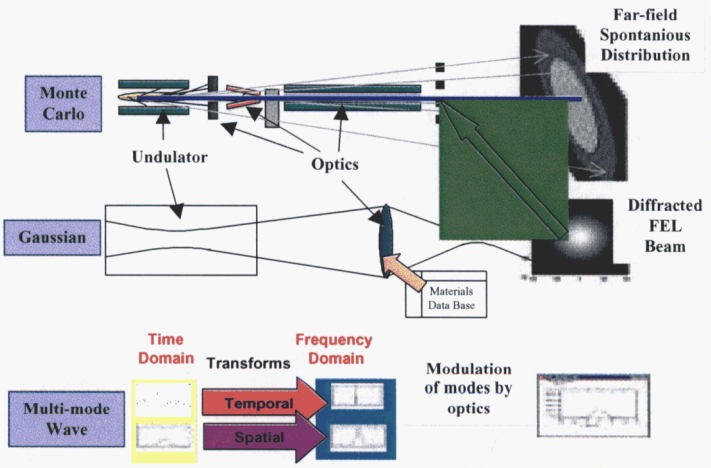

Figure 3.1 Simulation codes needed for the design of x-ray optics and diagnostics for fourth-generation light sources

Creating models and simulations of fourth-generation light sources is a challenging task. The fourth-generation light source emits both spontaneous radiation, which has a wide spatial and energy distribution, and FEL radiation which has a very small spatial and energy distribution. The models and simulations must take into account both wave effects and photon effects. The wave effects include diffraction as well as phenomenon associated with the very short, spiky, nature of the FEL beam.

Proper simulation of the fourth-generation light source requires three simulation codes as illustrated in Figure 3.1. The Monte Carlo shoots simulated photons through the optical elements in the beam. The photons suffer absorption, refraction at interfaces, and Compton scattering. Spontaneous photons are generated according to the far field distributions calculated with a wave model. The FEL photons are generated according to distributions calculated with other wave models. The chief wave model for calculating the parameters of the FEL uses a single Gaussian mode as a representation of the FEL. It calculates FEL distributions downstream of optical elements using Kirchhoff diffraction, and grating formalism. A more refined wave model uses input from the FEL simulation codes such as Ginger and Genesis [6,7]. The FEL simulations provide time-dependent electric fields at the undulator exit. The refined wave model separates the time-dependent field into time independent modes, calculates the effect of the optics on each

mode, then combines the results into a final electric field distribution downstream of the optics which can be fed into the Monte Carlo for further simulation.

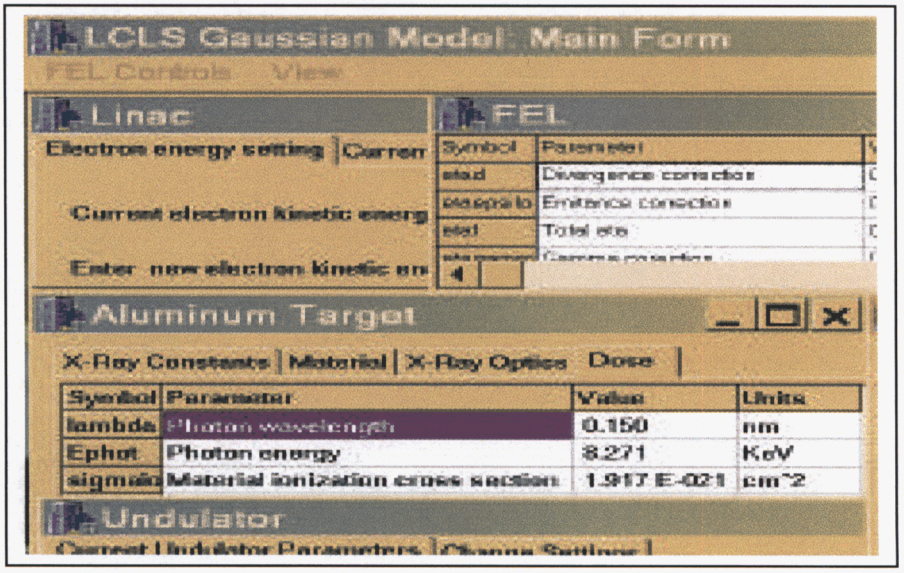

Figure 3.2 The single mode Gaussian beam simulator screen

The Gaussian Beam model, illustrated by the screen view in Figure 3.2, was written in FY 01. In FY 02 it was rewritten to conform to the Properties-Methods-Events (PME) C++ paradigm, and to interface with a database containing the optical constants for the materials. The new code has a stand-alone object for each of the components in the model. These components consists of the Linac, the FEL, the undulator, the Gaussian Beam, and a target material selected from the database. The PME paradigm allows these objects to be easily reused in other codes.

The "spontaneous" radiation emitted by fourth-generation light source is the normal synchrotron radiation emitted by an electron beam traversing an undulator. It is a large contributor to the backgrounds encountered in sensitive experiments. In FY 02 we developed a plan for simulating such radiation in the Monte Carlo. Since the fourth-generation light source undulators are very long the experimental halls are in the "near field" of the spontaneous radiation. Near-field simulation requires large amounts of computer time. Our scheme is to use the far-field radiation pattern, which is easier to calculate, as a template in the Monte Carlo for the angular distributions of simulated spontaneous photons generated randomly along the length of the undulator. The Monte Carlo then tracks these photons from their origin in the undulator to the desired position in the near-field, as illustrated by Figure 3.1.

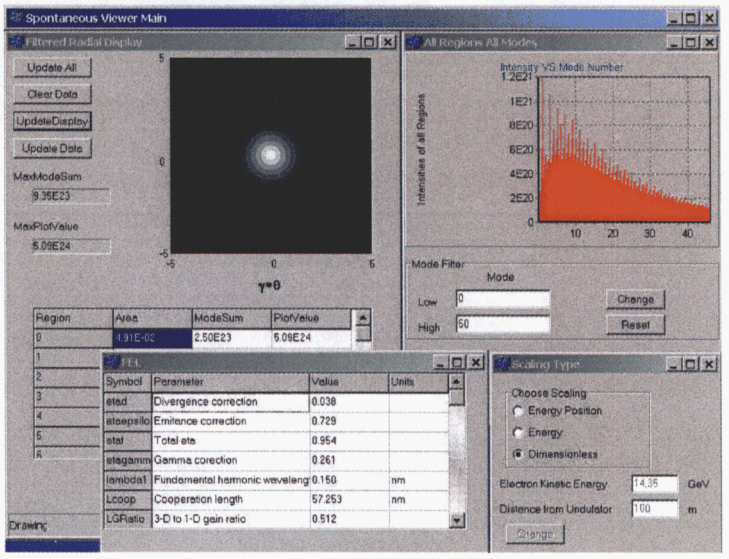

Figure 3.3 LCLS Far-Field Spontaneous Radiation Database Viewer

In FY 02 we obtained data on far-field distributions created by our SSRL collaborator Roman Tatchyn on the Cray computers at the NERSC facility at LBNL. The data set consisted of 1.3 million values for the spectral power-angular distribution of the spontaneous radiation spanning 23,000 photon energies and normalized to the electron relativistic boost factor g to save space. We inserted these values into a dynamic database and wrote PME modules to access in view this data. Figure 3.3 illustrates some of the modules. The module in the upper left is displaying the spatial distribution in $\gamma\theta$ space and its values in the table. The panel on the upper right gives the harmonic contents of the selected radiation in the spatial distribution. The panel on the lower right is used to change the scaling from the dimensionless $\gamma\theta$ coordinates to coordinates in space by choosing a particular electron kinetic energy setting for the Linac and a particular distance along the beam line. The panel on the lower left displays details about the Linac sentence.

In FY 02 we began work on the Monte Carlo simulation. Figure 3.4 shows the structure of the Monte Carlo objects and the user interface. The Monte Carlo makes full use of C++ class inheritance. The generator module, upper left, generates primary beam photons on demand. The base generator class, upper left panel, is overwritten to generate photons from the FEL, the spontaneous radiation interface, and other sources. The slab, top center, is derived from a basic materials/object class containing geometric and material data on objects placed in the beam. The sequencer, top right panel, directs the generation and tracking of photons through the simulation. The simulation results consist of photon distributions measured at various points along the beam line, lower left.

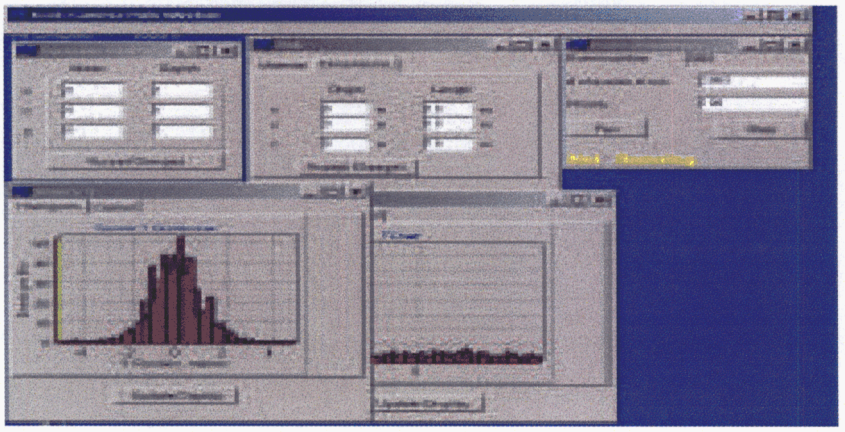

Figure 3.4 Monte Carlo simulation panels

4. Photon material interactions and damage

4.1. Theoretical

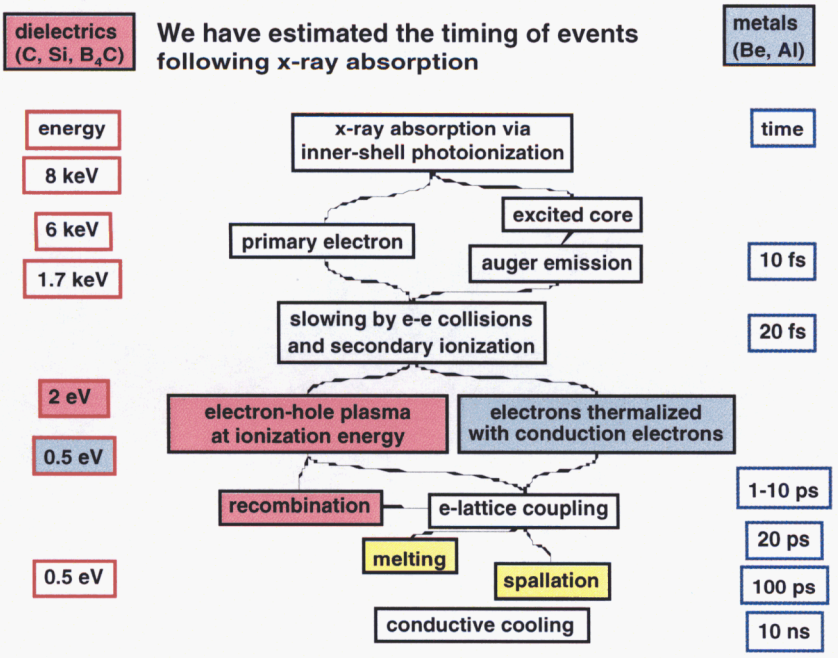

Figure 4.1 A summary of energy flows during x-ray - photon material interactions

Figure 4.1 illustrates the expected energy deposition processes for x-rays interacting with a low-Z solid [8]. Processes, typical time scales and typical energies (first x-ray, then electron, finally electron and ion), are shown for an 8 keV photon interacting with Si, one of the primary materials being considered for mirrors and diffraction crystals. The absorption of x rays proceeds primarily by inner-shell photo-ionization events, which occur essentially instantaneously. This is followed by the emission of a primary

photoelectron of energy about 6 keV and the creation of a core-excited atom. The atom relaxes mainly by the auger process in about 10 fs emitting an auger electron of energy 1.7 keV. Another auger process will lead to a lower energy electron and the creation of an atom with a valence-shell hole. The photo-and auger electrons then slow down by secondary ionization processes and by electron-electron (elastic) collisions. The slowing down is estimated to occur in about 20 fs, dominated by the highest energy electrons. This leads to an intermediate state of the matter with warm electrons (0.5 to 2 eV, at doses near the damage threshold). The actual temperature depends on the type of material; in metals, the energetic electrons will likely thermalize with the existing conduction band electrons, leading to a relatively low electron temperature, while in semi-conductors and insulators, the electrons will slow until they drop to the band-gap energy, at which they can no longer create new electrons. This energy is 2 eV in silicon. The thermalized electrons will then interact with the atoms and ions in the lattice on a much longer timescale. Recombination and electron-lattice coupling take place in 1-10 ps. Once the electrons and ions have equilibrated, bulk effects commence. The chief effects of interest are melting (timescale ~ 20 ps), and the propagation of stress pulses (timescale ~ 100 ps), which may lead to spallation or fracture. Cooling of the x-ray heated region occurs on a still longer timescale of about 10 ns, for a 1 μm deep deposition region, characteristic of grazing incidence x-rays. Thus damage is expected only after > 20 ps, well after the FEL pulse has gone, and a working assumption for precluding material damage that would affect x-ray properties is:

'There will be no changes to material x-ray properties during the x-ray pulse, and no irreversible changes at any time, as long as the fluence is kept < about 1/2 that required to bring the material temperature to melt' [9].

Figure 4.2 illustrates the situation at LCLS[1]; normal fluences (J. cm^{-2}) at the undulator exit far exceed those require to melt most materials. The problem is somewhat alleviated downstream, where the natural divergence of the beam (1 μrad at 8 keV, 10 μrad at 1 keV) reduces the fluence.

[1] optical quantities are taken from the CXRO home page at http://www-cxro.lbl.gov/, and physical constants from the CRC Handbook of Chemistry and Physics, 65th edition.

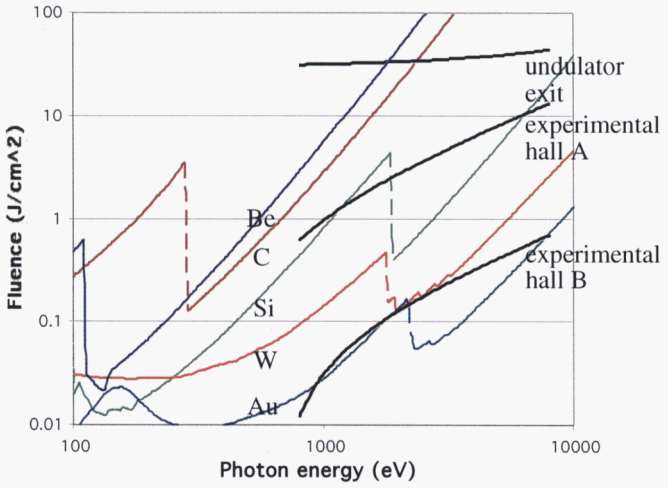

Figure 4.2 Normal incidence fluences from the LCLS coherent radiation beam, together with fluences required to bring various materials to their melting temperature (Be, C, Si, W, and Au). The phase change energy is not included. Curves are shown for the LCLS coherent beam at the undulator exit, and at positions representative of the two experimental halls.

The simple working criterion above assumes that long–time (i.e. > photon pulse length) irreversible processes such as phase changes (e.g. graphitization of C in multilayers, melt), spallation, and plastic deformation are precluded by keeping the material temperature below half the melting temperature, and that there are no short time (< photon pulse length) reversible or irreversible changes during the pulse itself. These assumptions are being explored, both theoretically and experimentally.

We have also considered thermal stresses that remain in a reflective x-ray optics long after the passage of an x-ray pulse (~ a few nanoseconds), when a mechanical equilibrium has already been established, but still before the heat has spread beyond the initially heated (~ 1 μm thick) layer. The stresses at this stage have a clear two-scale structure: the largest stresses are generated within a heated layer and the weaker ones extend to the distance comparable to the width of a beam imprint.

For some materials, even at modest temperature increase of the surface layer, the stresses may reach yield strength. Materials with a small thermal expansion coefficient and a large ratio of the Young's modulus to the yield strength (*E/G*) are preferable, as they would withstand higher energy depositions (in particular, beryllium is better than aluminum in this regard).

In the regimes where the yield strength is reached, the cycling will lead to cracking of the surface, probably, within a few hundred cycles At a high repetition rate (120 Hz) of the LCLS beam, the surface may become cracked and unusable for high-precision optics within less than a minute.

4.2. Experimental

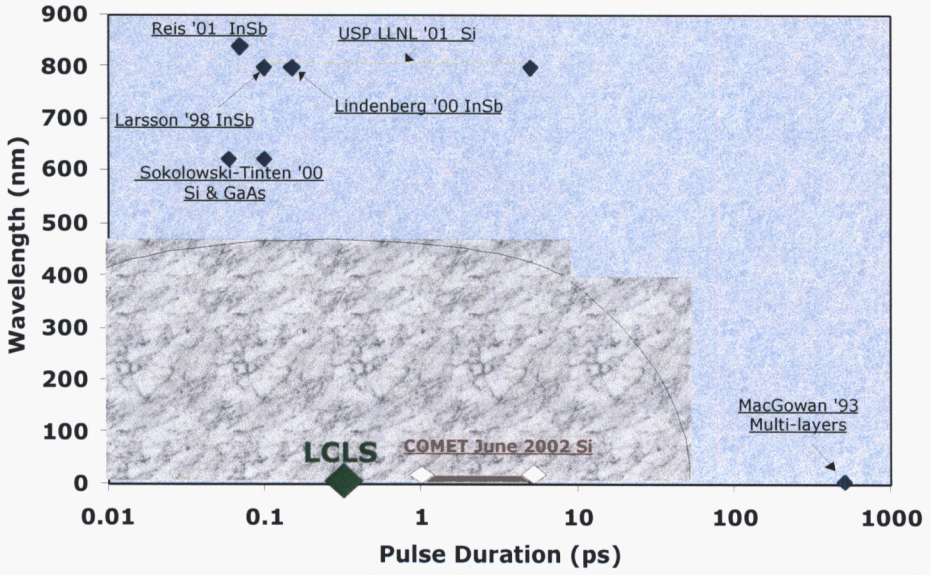

Figure 4.3 The region in wavelength – pulse duration space where damage experiments exist (blue background, with some specific examples shown), the region where no data exists (gray background), and the region where LCLS needs data.

Figure 4.3 shows where experimental data on material damage by photons exits, together with a large unexplored region that includes the LCLS operating points. Clearly further experiments are required. Consequently we initiated a research program under the LDRD project to investigate material damage effects.

Our experimental research on the interaction of photons with materials [10,11] proceeded along three major paths: (a) the interaction of 800-nm 100-fs high power laser pulses with silicon, (b) K-alpha source radiation production and its interaction with materials, and (c) the interaction of a transient picosecond x-ray laser at 14.7 nm with a multilayer. We carried out the following experiments:

(a) Irradiation of samples by an infrared short pulse laser:
Experiment at USP laser (LLNL) in 2001
(b) Irradiation from K-alpha sources
ATLAS 10 facility in Garching (Germany) – February/March 2002
JanUSP facility (LLNL) – July/August 2002
ATLAS facility in Garching – October 2002
(c) Irradiation by a transient x-ray laser
COMET facility (LLNL) – June/July 2002
Total (b) +(c): 12 weeks

The major results

We first investigated the possibility of simulating LCLS-like conditions with visible laser sources. It is possible in principle to simulate the x-ray grazing incidence energy fluence using visible laser radiation; a careful choice of materials allows one to match the normal incidence visible photon energy deposition depth to the grazing incidence x-ray photon deposition depth. Next we considered the use of an existing x-ray source, albeit not in the LCLS-relevant photon energy range, and Table 4.1 summarizes the parameters of some of those available. Modeling suggested that with relatively modest focusing, the COMET 147 Angstrom table-top x-ray laser (focal spot 10-20 micron) could be used to reach and surpass the fluence threshold for optics damage in silicon. An experiment was developed to achieve and demonstrate this. A multilayer optics element was used as a target. Finally we considered the use of K-alpha sources driven by visible lasers, to produce LCLS-relevant photon energies.

TABLE 4.1 COMET, Capillary and DESY VUV-FEL x-ray laser source parameters

Source Parameters	COMET x-ray Laser	Capillary [b] x-ray laser	DESY VUV-FEL[c]
Pump Energy – laser or condenser (for capillary) (J)	5 – 10	40-100	-
X-ray Laser Energy (μJ)	25	100-900	300
Photons/Shot	2×10^{12}	2×10^{14}	10^{13}
Shot Rate (Hz)	0.004	1-10	10
Wavelength (nm)	12 – 47	47, 53, 61	6
$\Delta\lambda/\lambda$	10^{-4}	10^{-4}	6×10^{-3}
Source Dimensions (μm)	25 by 100	3×10^{-2}	150
Divergence (mrad)	2.5 by 10	2-5	0.06
XRL Pulse Duration (ps)	2 – 25	700 – 1500	0.1

[a] Units of ph. mm^{-2} $mrad^{-2}$ s^{-1} $(0.1\%\ BW)^{-1}$; [b] parameters shown are for the 46.9nm Ne-like Ar laser; [c] Expected start operation 2005

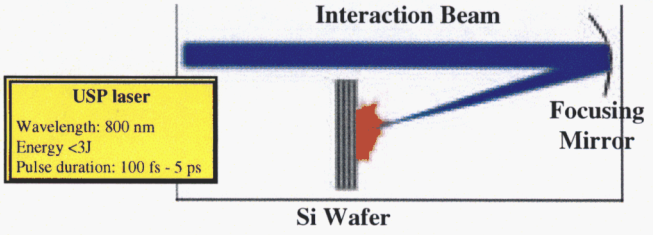

Figure 4.4 An illustration of the geometry used in the visible surrogate damage experiment.

a) Visible surrogate: A single Si crystal (111) was irradiated by 800 nm converging laser beam pulses under normal incidence. Pulse lengths were varied between 100 fs and 5000 fs, with fluences up to ~0.3 J cm^{-2}. After irradiation the samples were examined microscopically and numerically evaluated, as well as by AFM, x-ray topography, differential interference optical microscopy and sputter auger electron microscopy. The data, summarized by Figure 4.5, show clearly observable irreversible damage at fluences

as low as ~0.1 J cm^{-2}, with no significant dependence on pulse duration within the range studied. The pulse duration was varied by a factor of more than 100 while keeping the energy constant; the damage onset fluence remained unchanged. This onset fluence is 50 times lower than that predicted from the linear absorption coefficient (800 cm^{-1}) using the classical Drude's theory, which gives satisfactory results for previous long pulse damage experiments. Attempts to explain this discrepancy, including modifying the plasma production and ablation theory that has fitted previous high power, short pulse, lasers ablation [12], have not met with success.

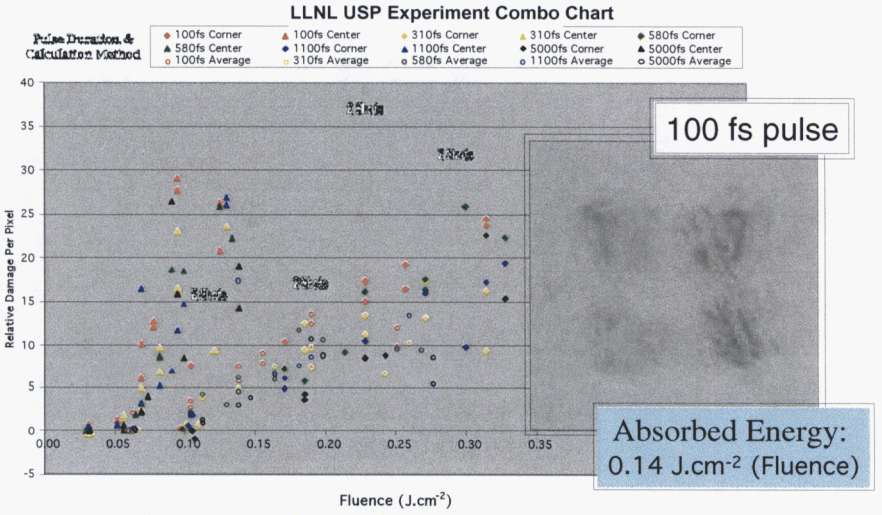

Figure 4.5 Results from the visible photon damage experiment, showing a measure of the damage as a function of fluence. The inset shows the damage pattern, a result of the near field diffraction pattern associated with an aperture in the system

b) K-alpha sources: A variety of K-alpha sources generated by a short (100 fs – 1 ps) laser pulse have been studied. The available wavelength range is from 1.5 keV (for Al target) to 8.0 keV (for Cu) as demonstrated and optimized during a first Garching experiment. The damage experiment uses such a K–alpha source to irradiate (in back-emission) a sample material (See Figure 4.6). The advantages of this scheme are the short wavelength (comparable with the projected 4th generation X-FEL facilities), and the short pulse duration achievable. The disadvantage is the complexity.

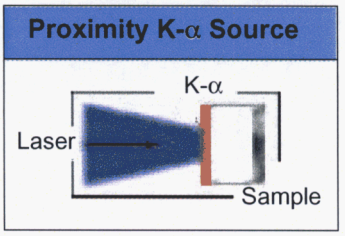

Figure 4.6 An illustration of the K-alpha x-ray photon production and damage experimental layout

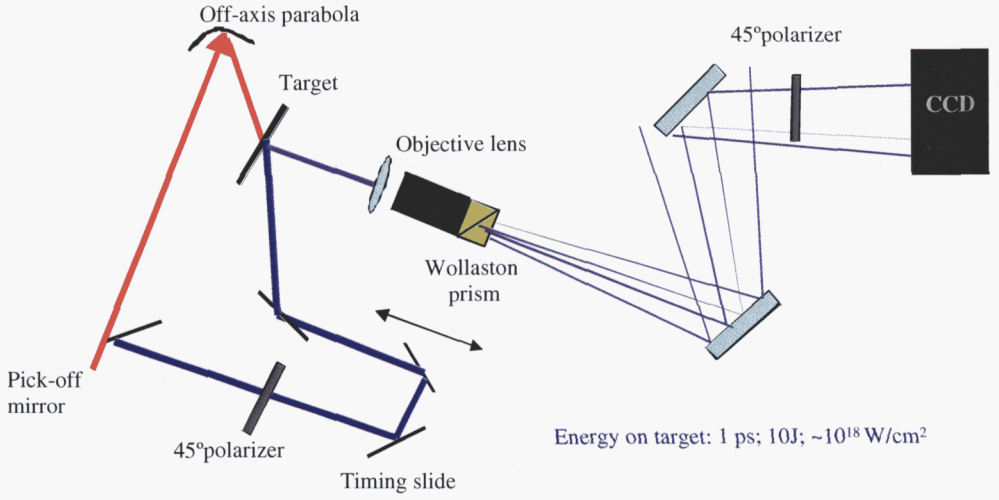

Figure 4.7 The geometry of the damage experiments using the K-alpha source, with the viewing geometry

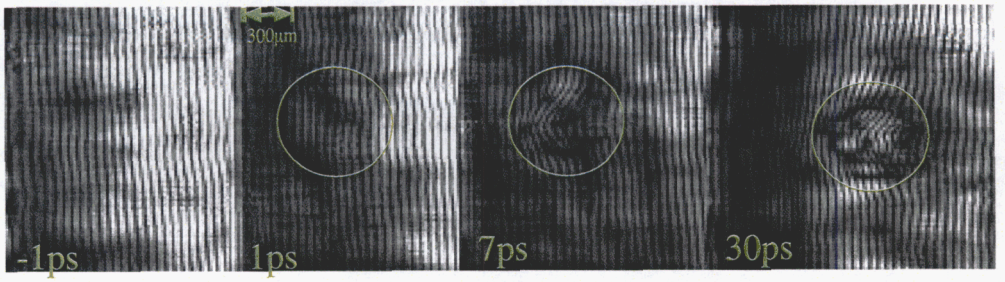

Figure 4.8 Initial results, with a 10x magnification onto 1" CCD and a 800 nm probe

The first specific damage experiment was carried out at the JanUSP facility, using the geometry of Figure 4.7. The JanUSP laser ~10 J, 1-ps pulse was focused to a 50 micron spot size on a target. The target was composed of a 20 micron Si K-alpha source (1.7 keV) and a 1 micron Al sample separated by a 20 micron vacuum gap. The back surface of the sample was probed by a laser beam that was picked-off as a small portion of the main beam. The reflected probe beam was examined by a Nomarski-type interferometer. The first results, as depicted in Figure 4.8, show a significant sample surface modulation after a shot. The damage appears as soon as 1 ps after the onset of the main pulse and it increases with time. The early damage onset is a signature of damage caused by x-rays. The significant increase in damage at timescales up to 30 ps suggests also that other mechanisms are involved, including damage by protons or possibly even hot electrons. The proton emission that originates from adsorbed CH on the target front surface was recorded and confirmed using a radiochromic film. The role of hot electrons will be examined in our upcoming experiment at the ATLAS facility (Garching, Germany).

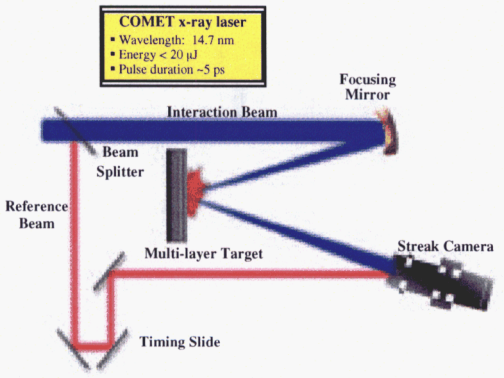

Figure 4.9 An illustration of the x-ray laser damage experimental layout

c) x-ray laser: The first such experimental campaign concentrated on the x-ray laser temporal characterization. The experimental configuration is shown in Figure 4.9. The pulse duration at optimal pumping conditions was measured to be (2.2±0.5) ps, in agreement with previous measurements. The dependence of x-ray laser conditions on the pump laser duration was also studied. The experiment shows that the x-ray pulse duration can be controlled by the pump laser pulse duration, from ~ 2 ps up to (6.0±0.5) ps for a 5 ps pump. This result is important not only for the damage studies but also because it demonstrates intrinsic pulse duration control.

Fluences of ~0.02 J cm^{-2} were directed onto a multilayer target, as shown in Figure 4.9. Any damage (e.g. change in multilayer depth) is then observed as a change in reflectance angle. Some indications of damage at this very low fluence were seen, but the experiment needs repeating before a definitive statement can be made concerning fluence to damage.

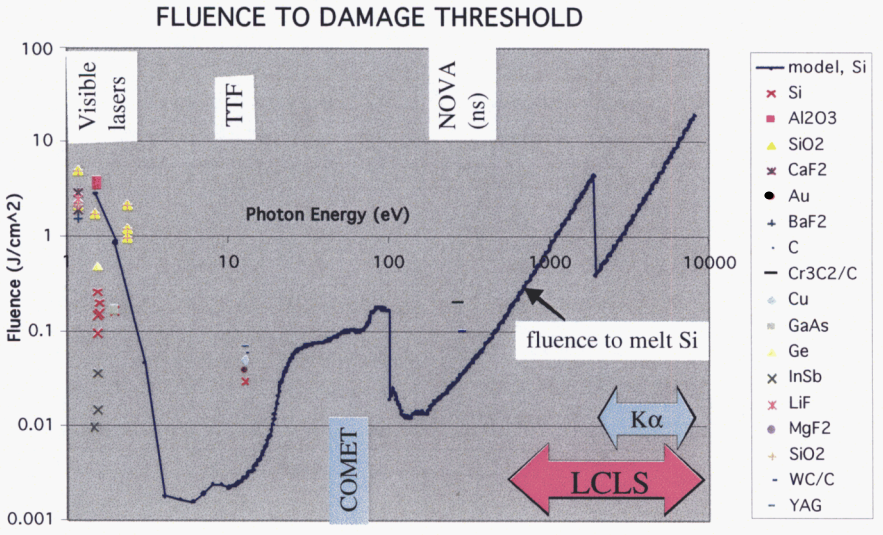

Figure 4.10 The fluence to damage for a variety of materials, as found experimentally at different photon energies. The blue curve is the simple thermal melt line for Si. The photon energy values associated with various sources are indicated.

d) Summary of experimental data: The data we have gathered from the visible light (~ eV) x-ray surrogate experiments, interpreted as a fluence to damage, are not consistent with the simple picture expected for x-ray damage. Other published data for different wavelengths and materials, summarized in Figure 4.10, is inconclusive; some data is consistent with thermal melting, while some is not. The data for Si, shown as red x's, can lie above or below the simple estimate, depending on the photon frequency and material. The first experiments we have attempted using x-ray photons to damage have not yielded clear results. Clearly more experiment and theory are required before a definitive constraint on fluence can be supplied for LCLS optics design.

5. X-ray optics development

To deal with the very high fluences, a variety of techniques are proposed for optics design, including [6,7,9] a far field experimental hall to reduce energy densities by natural divergence, a gas absorption cell [13] to continuously attenuate by > 10^4 , low-Z optics [14] that are damaged least (e.g. a phase zone plate for warm dense matter experiments), and grazing incidence optics that increase the optical footprint and reflect most incident power [6,7,9]. In most cases the experiments that require the most challenging beam manipulation, including time compression, time slicing, beam splitting and beam delay, are planned for the far hall. Should these hardware solutions be insufficient, two other categories are being explored. First, non-solid state (i.e. liquid and

plasma) optics that are readily replenished have been studied. Second, there is always the option of dynamic solid-state optics, that are spatially translated between shots

5.1 High resolution multilayers

A series of multilayer optics, suitable for time slicing, have been designed, built and tested. The conclusions are:

The SSRL beamline can be used as a high precision calibration facility for multilayer mirrors

B_4C-C multilayers are restricted in applicability by their half life at room temperature, ~ 1 month

A variety of WSi_2Si and MSi_2S multilayer mirrors worked almost as well as predicted at 8 keV. One MSi_2Si layer, (see Figure 5.1) had a $E/\Delta E = 292$, and $55 < R < 67$. This leads us to expect to be able to produce mirrors suitable for wavelength filtering and time slicing for LCLS (requiring $300 < E/\Delta E < 1000$).

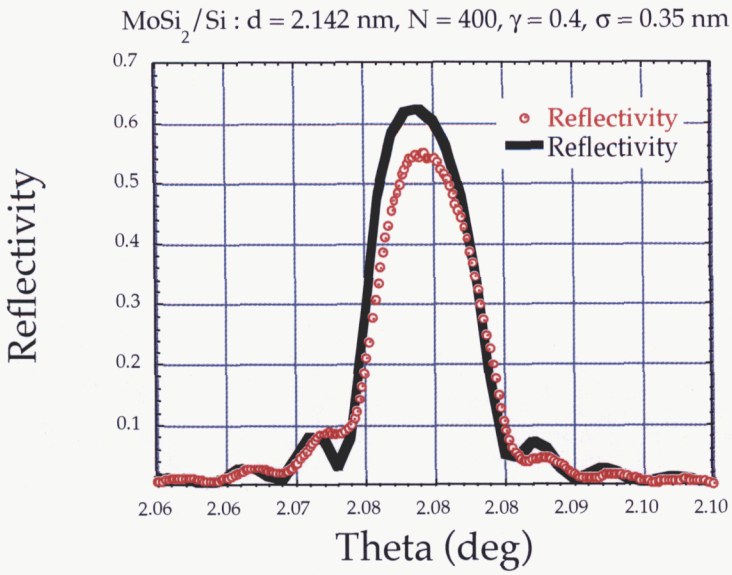

Figure 5.1 A comparison of theoretical (red) and experimental(black) reflectivities for an LCLS- relevant multilayer

5.2 Grazing incidence optics

At the location of Hall A, focusing with a transmissive lens might be possible using the lowest Z materials. However the margin of safety is very small, and with multiple shots the temperature increase becomes a problem. Instead we propose to use grazing incidence mirror geometry; an ellipsoidal or parabaloid surface focusing in two dimensions. The absorbed energy per atom is given by

$$\eta = \frac{E_{beam} Sin(\theta_i)(1-R)}{d_w^2 \delta n_a}$$

E_{beam} is the beam energy, d_w the beam diameter at the optic, θ_i the grazing incidence angle, δ the penetration depth (approximated by the maximum of the 1/e penetration depths of the light and subsequent photo-electrons) into the material in a direction normal to the surface, n_a the atomic density of the material, and R the reflection coefficient. As the grazing angle is decreased the reflectivity term (1-R) and the footprint term $Sin(\theta_i) / d_w^2$ decrease the absorbed energy density. Until the critical angle is reached (from above) the penetration decreases, so this term increases the absorbed energy density.

The material is chosen to accommodate the high fluence, so must be low Z. Figure 5.2 shows the ratio of energy absorbed per atom at a given grazing angle to that absorbed for normal incidence, for Si at both 0.8 and 8 keV. Large reductions are possible below the grazing angle. Including an estimate for the photo-electron penetration depth shows that an order of magnitude reduction from the marginally safe energy load is possible at 1 degree.

The proposed design is for a Be, C or Si parabaloid lens with grazing incidence angle 1 degree, distance to focus of 1 m, and thus a radius $r = \sqrt{1.2188 \times 10^{-3} z}$ (m) (= 3.5 cm at the center of the beam). The full-width-half-maximum beam diameter, ~ 650 μm for 1 keV photons at the experimental location, implies a mirror length ~ 7 cm. To achieve the 0.1 um spot diameter implies a surface finish ~ 5 nm, a maximum slope error ~ 0.5×10^{-7} rad, and a maximum tilt of the axis of 1×10^{-5} rad. The maximum slope error, beyond state of the art, is relaxed to present capabilities for the 1 um spot diameter.

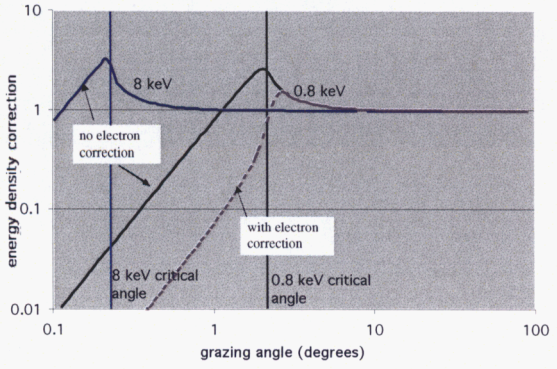

Figure 5.2 The multiplicative factor on the tolerable fluence as a function of grazing incidence angle, for a plane Si surface irradiated by 800 and 8000 eV photons. For 800 eV the results are shown with and without a correction for photo-electron penetration. The critical angles are marked as vertical lines.

Two techniques are considered for manufacturing the optic. First only that part of the parabaloid that will reflect the photons can be constructed, i.e. a section ~ 7 cm long by ~ 1 mm wide. This can be made by numerical machining, an expensive process if large numbers of lenses are required. Alternatively full parabaloids can be made by sputter depositing layers of materials (e.g. Be, or C) onto a super-smooth mandrel, thus forming an optic from the inside outward. When the mandrel is separated from the sputtered foil, the innermost layer replicates the mandrel smoothness and serves as the reflecting surface. The focusing element is thus a tube that is open at both ends, as shown in Figure 5.3. X-rays enter one end, undergo a single reflection at the interior surface, and exit from the other end with a different direction of travel. It may also be possible to form a Si optic using a mandrel rotated into a Si block.

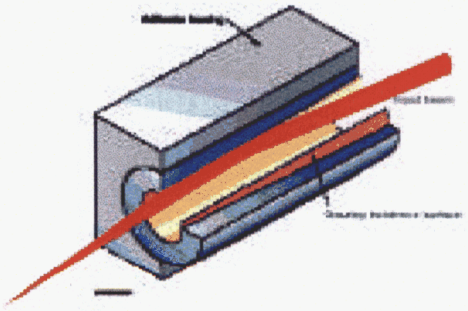

Figure 5.3 A schematic drawing of a replicated parabaloid lens, used for focusing.

Stress-relieved specular (and if required multilayer) reflecting surfaces and supporting electroplated shells do not deform during the separation process and consequently produce super-smooth surfaces comparable to the initial mandrel surface (i.e. rms ≈ 3 to 4.5 Å) with figures replicating the mandrel figure. In principle, single layer specularly reflecting surfaces only require that the total thickness of the single reflecting media layer be controlled for effective reflection performance to be achieved. In practice, it is necessary to maintain surface roughness and composition at levels which are technically required for effective performance. Calibration, in this case, requires only a quantitative knowledge of the layer thickness deposited on the replication mandrel surface under specified deposition source and replication mandrel motion conditions. Typical specular reflecting material structures are between 25 nm and 50 nm thick. Focusing for the atomic physics experiments may be achieved using a parabaloid mirror. Two techniques are considered for manufacture. First, only that part of the parabaloid that will reflect the photons can be numerically machined, i.e. a section ~ 7 cm long by ~ 2 mm wide. Alternatively full parabaloids can be made by sputter depositing layers of materials (e.g. Be, or C) onto a super-smooth mandrel, thus forming an optic from the inside outward. During mandrel removal, the stress-relieved specular (and if required multilayer) reflecting surfaces and supporting electroplated shells do not deform, and consequently produce super-smooth surfaces comparable to the initial mandrel surface (i.e. rms ≈ 3 to 4.5 Å) with figures replicating the mandrel figure. It may also be possible

to form a Si optic using mechanical-chemical polishing. Stress-relieved specular (and if required multilayer) reflecting surfaces and supporting electroplated shells do not deform. Typical specular reflecting material structures are between 25 nm and 50 nm thick.

In addition, a related micro-lens for the same purpose has been designed, that is predicted to survive if built from Be, C or Si. A general view is shown in Figure 5.4; the central peak represents the focused light.

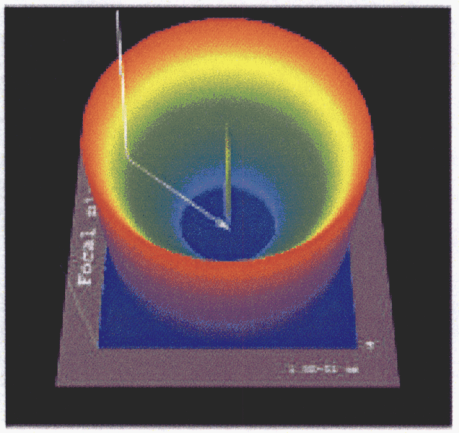

Figure 5.4: a view of a 100 mm x 40 mm x 8 mm micro-lens designed for the atomic physics experiments

5.3 BeB compounds

A suitable material for high fluence optics is Be, because of its low photo-absorption cross-section and high melting point. Unfortunately, pure Be (devoid of impurities as oxygen which is found in the powder processed materials) is a brittle material and susceptible to machining damage that can lead to degraded properties particularly under high strain rate conditions [15]. One possibility to overcome this limitation is to refine the grain size in order to prepare a more homogeneous and isotropic material for processing to a high surface finish. The synthesis of Be-B compounds as vapor deposited coatings have shown great promise in reducing grain size to the *nano* scale [16]. For bulk applications of interest, two Be-B compounds (with 3% and 10% B) have been vacuum cast and slow cooled for application consideration as mirrors. Although the grain size is reduced by more than a factor of three for the Be-3%B sample in comparison to the 100μm grain size for the cast pure Be as shown in the optical micrographs of Figure 5.5, the grain size remains larger than desired for low rms roughness surfaces. A possible path to simulate the nanoscale grain size and surface roughness results for vapor deposited coatings is to greatly increase the quench rate of the vacuum casting.

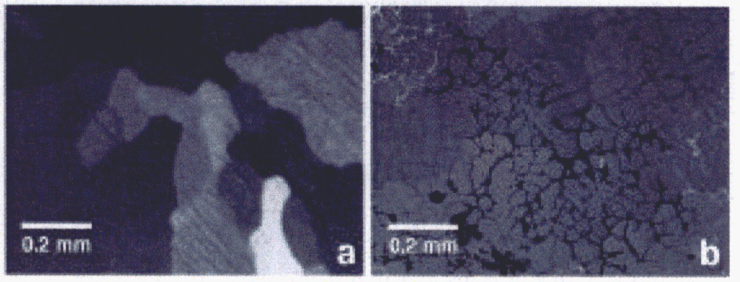

Figure 5.5 Vacuum cast samples of (a) pure Be and (b) Be-3%B are imaged using polarized light after being prepared in cross-section by mechanically grinding using SiC then rough-polished using a colloidal suspension of diamond particles.

5.4 Low-z phase zone plates

Low-z transmissive optics may be used at the higher photon energies even at the undulator exit; even with 100% absorption and normal incidence the lowest Z materials will not melt. Phase zone plates, produced by sputtering and then slicing, have already been successfully used[9] in the hard x-ray regime (> 5 keV), so that their use is considered a variant on a proven technique.

Figure 5.6 shows details of a design. The lens is carved into the face of a C disk and mounted over a hole drilled through a 25.4 mm diameter Cu mount. The C disk is 650 μm thick except in the center, where it thins down to 400 μm. The active portion of the lens is 200 μm in diameter and consists of 6 concentric grooves machined to a maximum depth of 18.8 μm. The plot of the beam profile at the lens, Figure 5.6g, shows that the 200 μm lens diameter captures most of the beam.

The shape of the grooves was determined by calculating the phase change necessary to convert the diverging Gaussian XFEL beam from the undulator to a converging Gaussian waveform whose waist is at the sample position. The radial phase profile was converted to a depth profile by multiplying by the optical constant for C which, at 8.275 keV, is 18.8 μm / 2π.

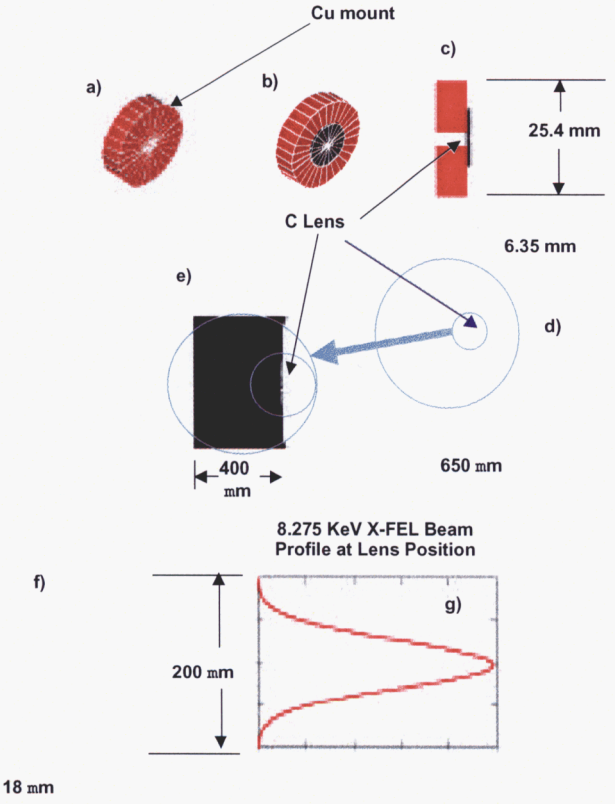

Figure 5.6 Details of the warm dense matter (plasma experiment) lens design. a) the Cu mount, b) the Cu mount and lens, c) another view of the mount and lens, d) an enlarged view of the center part of the mount and lens, e) the C lens (before thinning), f) detail of the lens surface, g) the FEL beam profile shown on the same vertical scale as the lens detail in f.

A radiograph is shown in Figure 5.7 of an aluminum version that has been successfully tested. The lens is carved into the face of a C disk and mounted over a hole drilled through a Cu mount. The C disk is 650 μm thick except in the center, where it thins down to 400 μm. The active portion of the lens is 200 μm in diameter and consists of concentric grooves machined to a maximum depth of 18.8 μm.

Figure 5.7 A radiograph of an Al Fresnel lens, with feature size ~ 10 μm, groove depth ~ 20 μm

5.5. Gas attenuator

Attenuation of the beam is accomplished by passage through a gaseous, solid, or liquid medium. While all have been considered, the nominal design [13], shown in Figure 5.8, is for a gas cell operated with high pressure puff valves to introduce the absorbing gas into the path of the coherent FEL photons. At the lower photon energies, gas must be used as all solid materials will melt. One possibility under consideration is to use a mixed attenuation scheme; gas for initial attenuation, followed by low Z (e.g. Be) for further attenuation. This would have the advantage of reducing the gas handling requirements.

The axial dimensions and the number of valve nozzles must allow a sufficient depth of the gas to provide four or more orders of magnitude of attenuation over the full range of the LCLS fundamental (~0.8 to 8 keV). The combined axial and transverse dimensions are determined by the requirement of maintaining an average vessel pressure of <0.0075 Torr, corresponding to the Knudsen-through-molecular flow regimes[8]. This pressure, (for N_2) is sufficiently low to be reduced to $<10^{-6}$ Torr by the differential pumping sections bracketing the chamber.

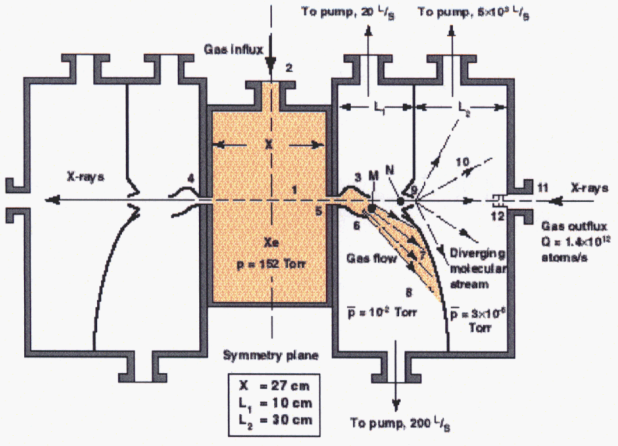

Figure 5.8. The conceptual design for the gas cell absorber.

This component will be capable of continuously attenuating the coherent intensity at 8.3 keV from full strength to 4 orders of magnitude below peak. The attenuation range will be 6 orders of magnitude at 830 eV. This attenuator will be used to reduce the LCLS fluence to below damage thresholds for those instruments and experiments that will not require the full output power of the LCLS. Its conceptual design is complete.

5.5 Solid Attenuators

Further from the undulator it is possible to utilize solids for attenuation. A design that will meet the fluence constraints using multiple materials is illustrated in Figure 5.9.

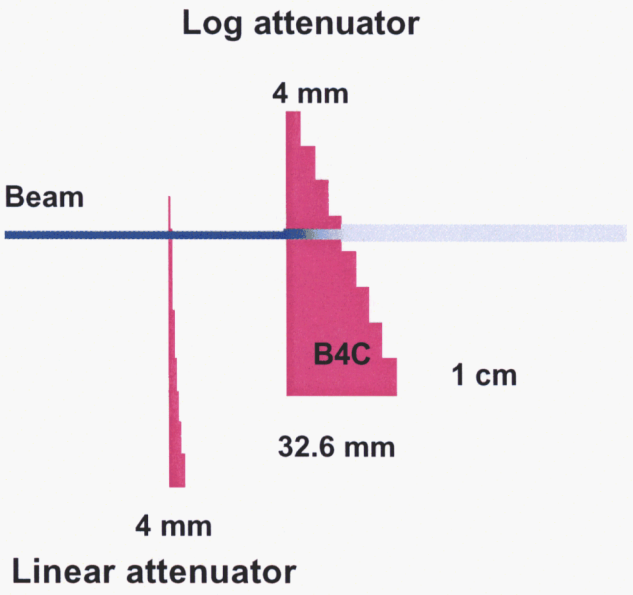

Figure 5.9 A design for a solid attenuator that meets fluence limitations away from the undulator

5.7 Novel concepts

5.7.1 Plasma optics

Capillary discharges produce plasmas with density profiles suitable for focusing. The capillary material supplies the plasma, which is Joule heated in the center and cooled at the edge. Pressure balance provides the inverted density profile. A design study [19] for such a transmissive system based on LiH as been completed, and shows it could work in the 3 to10 A region with the full fluence, with focal spot sizes < 1 μm, lasting for > 10^3 shots.

5.7.2 Liquid optics

A new class of high-flux renewable liquid optics is proposed, with size from a fraction of a cm to a few cm [17]. Working fluid is pressed by a piston through a porous substrate (e.g. fused capillaries) to form a film, ~ 10 to 100 μm thick. After the FEL pulse, the film is sucked back through the substrate by a reversed motion of the piston, and formed anew before the next pulse. The working surface of the film is maintained parallel to the substrate by capillary forces. A properly made film can be arbitrarily oriented with respect to the gravitational force, and controlled by electrostatic and magnetic forces, allowing one to make parabolic mirrors and reflecting diffraction gratings.

5.7.3 Thermo-elastically controlled optics

Consider a polished flat metal surface that has a sufficient reflectivity for x-rays at a grazing incidence. This is then irradiated by a subsidiary optical or UV laser pulse, at an angle near normal, and with wavelength corresponding to as strong as possible surface absorption. The subsidiary laser heats the metal surface in a desired surface pattern, and thermal expansion creates a desired surface relief - a focusing or defocusing mirror. If after the passage of the main FEL pulse the surface is damaged, the mirror plate can be translated. A preliminary design study shows that a 10 W, 10 mJ laser could produce a focusing mirror on an Al plate

6. X-ray diagnostics development [18]

6.1 Direct Scintillation Imager

A Direct Scintillation Imager has been constructed and successfully tested, as shown in Figure 6.1 It is an insertable, high-resolution scintillator viewed by a CCD camera for measuring spatial distributions and for alignment and focusing of optical elements. Traditional instruments have used phosphorus screens to convert x-rays to visible light that can be recorded by a CCD. Even with a microscope objective to magnify the screen, the spatial resolution is limited by the spatial resolution of the phosphorus that is typically in the range of 10 to 50 microns. Such resolutions are of marginal utility to the LCLS, which has a beam diameter at 8 keV of 100 microns. Recently, workers at the ESRF synchrotron facility have used thin-film single-crystal scintillators for x-rays, achieving 0.8 micron resolution. The scintillator is a 5 micron thick Ce doped YAG crystal on a 100 micron YAG substrate. Other crystals such as LSO are likely to work as well. The gated-intensified CCD camera can be read out at 120 Hz, providing pulse-to-pulse information.

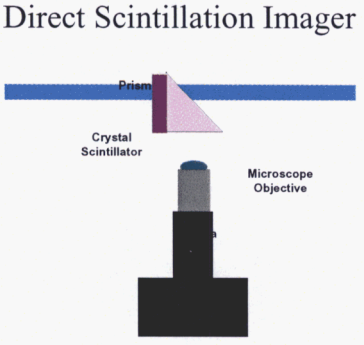

Figure 6.1a Direct Scintillation Imager

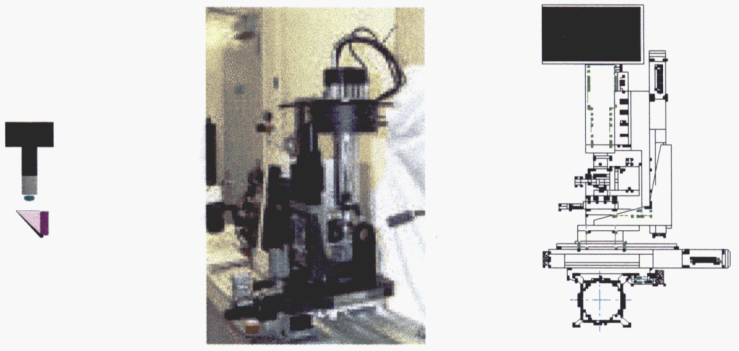

Figure 6.1b Direct Scintillation Imager, as built and tested

The Direct Scintillation Imager is intrusive – it blocks the beam. Its wide field of view will allow viewing of the spontaneous radiation pattern. In addition, its scintillator is susceptible to damage at the full FEL intensities.

6.2 Scattering Foil Imager

The Scattering Foil Imager (Figure 6.2) overcomes the FEL damage problems of the Direct Scintillation Imager by utilizing a thin foil of a low-Z material such as Be to act as a beam splitter to partially reflect a portion of the beam onto the YAG imaging camera which remains out of the beam. The reflected intensity can be adjusted by changing the angle of incidence. A reflectivity of 10^{-4} can be obtained with an incident angle of 1° at 8 keV and an incident angle of >2° at 0.8 KeV. The major foreseeable problem with this concept is the background x-ray radiation impinging on the crystal due to Compton scattering of the FEL beam by the Be foil, and any fluorescence from an oxide layer on the foil surface.

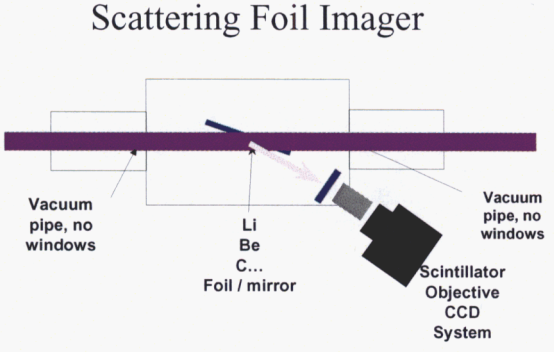

Figure 6. Scattering Foil Imager

With a thin (30 micron) polished Be foil, the Scattering Foil Imager is nearly transparent to the 8 keV radiation and can be used throughout the beam line as a non-intrusive pulse-to-pulse monitor of the beam energy, shape, and centroid. At 0.8 keV, the foil will not be transparent but the (Be) foil will be able to withstand the full FEL intensity so the Scattering Foil Imager can be used intrusively to measure the pulse-to-pulse statistics of the beam energy, shape, and centroid.

6.3 Micro-Strip Ion Chamber

The Scattering Foil Imager cannot monitor the 0.8 keV FEL non-intrusively since it is opaque and even at 8 keV it could introduce unwanted distortion into the beam. A traditional ion chamber, commonly used at current synchrotrons, is designed to operate at 1 atmosphere gas pressure, with a fairly low intensity DC beam. The high intensity and pulsed nature of the FEL require some modifications to the traditional design (see Figure 6.3). The current-measuring electronics of traditional ion chambers must be replaced by pulse processing electronics to measure the energy in each FEL pulse. The drift region must be carefully designed so that the photo-electrons from the pulse are efficiently collected at the anode in the time between pulses. The chamber must be operated at pressures below 1 atmosphere to reduce the instantaneous charge that must be drifted and collected. At 8 keV the gas can be contained within Be windows, but for 0.8 keV operation a windowless chamber with differential pumping is required. Finally low-resolution centroid and shape information can be obtained by segmenting the anode as in a micro-strip detector.

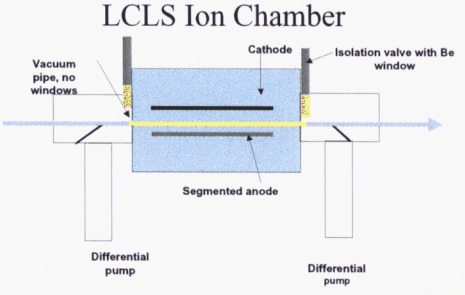

Figure 6.3 LCLS Ion Chamber

Because of the statistical nature of the FEL radiation it is very important to monitor the beam energy, centroid, and overall shape on a pulse-to-pulse basis in a non-intrusive manner. The micro-strip LCLS Ion chamber offers less-intrusive monitoring of the FEL pulse-to-pulse energy as well as low resolution centroid and shape information. Figure 6.4 shows the principles of the micro-strip readout.

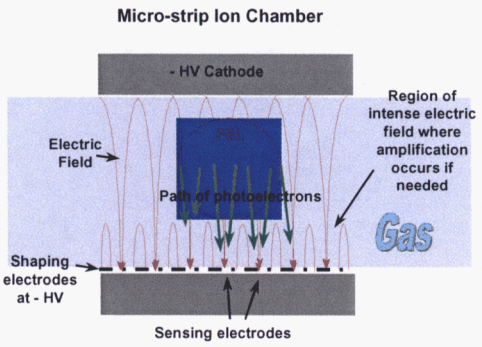

Figure 6.4 Micro-strip Ion Chamber

Photoelectrons liberated by the FEL photons drift down to thin sensing electrodes lithographed onto a substrate. In between the sense electrodes are thicker strips at negative high voltage, which shape the drift field. The centroid and shape are determined by the distribution of charge collected on the sense strips. At sufficient voltage and using correct gas, the electric field in the region near the sense strips can be high enough for gas multiplication to occur. In this regime the sensor is sensitive to single photoelectrons. This could be an advantage for operation at 0.8 keV, since it would then be possible to lower the gas pressure considerably and reduce the pumping load.

6.4 Total energy

It is desirable to measure the FEL pulse energy utilizing calorimetric techniques to avoid any reliance on the theory of photon-atom interactions at LCLS intensities.

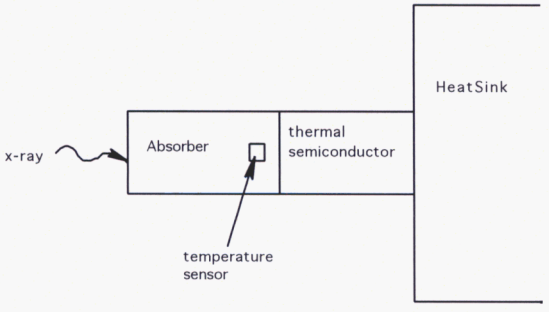

Figure 6.5 Calorimeter for accurate pulse energy measurement

The calorimeter (Figure 6.5) has a small volume x-ray absorber which absorbs all of the x-ray energy resulting in a rapid temperature rise. The heat capacity and mass of the absorber determine the temperature rise. For a 1% measurement, the thickness of the absorber must be at least 5 mean free path lengths in order to capture better than 99% of the x-ray energy. The sensor measures the temperature rise of the absorber. The thermal

mass of the sensor is small compared to the absorber. The heat in the absorber is conducted through the thermal weak link to the heat sink. The purpose of the thermal weak link is to delay the heat transfer from the absorber to the heat sink long enough to measure the temperature rise in the absorber. The heat sink is held at a constant temperature. The energy deposited by the x-ray is conducted into the heat sink before the next x-ray pulse. The thermal conductivity of the absorber, the thermal conductivity of the thermal semiconductor, the geometry of the absorber, and the geometry of the thermal weak link control the rate at which the heat in the absorber is conducted to the heat sink.

For 8 keV operation the absorber will be a Si cylinder 0.5 mm in diameter and 0.5 mm thick. The 0.5 mm thickness is > 5 attenuation lengths and the 0.5 mm diameter nicely accommodates the ~340 microns FWHM diameter of the 8 keV FEL at the position of the commissioning diagnostics tank. The dose at 8 keV to Si in this position is 0.12 eV/atom, which is acceptable for a simple absorber.

For 0.8 keV operation the absorber will be a Be disk 3 mm in diameter and > 25 microns thick since the dose to Si at this wavelength is too high. The 3 mm diameter is necessary to contain the 0.88 keV beam whose diameter at this position is 1.9 mm FWHM.

The calorimeter will be positioned on the "optics stage" in the commissioning tank allowing it to be aligned utilizing the rear imaging detector.

6.5 Pulse Length

Measuring the 233 fs pulse length is perhaps the most challenging measurement at the LCLS. Several concepts have been proposed, all involving a medium which modulates an external laser beam when exposed to the x-ray FEL. The method we have chosen to baseline is illustrated in Figure 6.6. The beam from a 1500nm CW laser is split and made to pass through the two arms of an interferometer patterned in GaAs on a substrate. X-rays impinging on one of the arms changes its index of refraction causing a modulation in the CW beam after it is recombined. The modulation of the CW beam is in principle of the same duration as the x-ray pulse and can be measured with a streak camera to >200 fs. To achieve better temporal resolution, the modulated CW beam is sent through a "time microscope" which stretches the pulse by a factor of 2 to 100 x. The stretched pulse length is then measured with the streak camera.

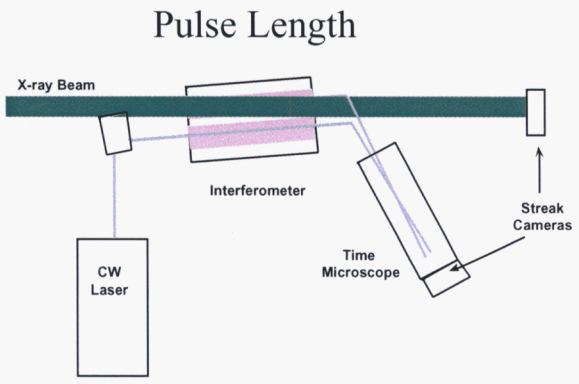

Figure 6.6 Pulse length measurement

The device can also be used to synchronize an external laser pulse with the x-ray beam. This is accomplished by feeding the external pulse through the time microscope alongside of the x-ray modulated CW pulse and measuring both on the same streak camera.

6.6 Photon Spectrum

The commissioning diagnostic tank is converted into a spectrometer by adding a crystal at 8 keV or a grating at 0.8 keV. In either case the optic disperses the radiation onto the x-ray sensitive region of a fast readout position-sensitive detector.

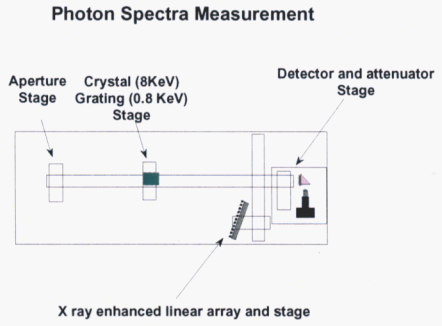

Figure 6.7 Spectrum measurement

6.7. Transverse coherence

The transverse coherence will be measured in the commissioning diagnostics tank using the setup shown in the figure that employs an array of double slits with constant slit width but different slit spacings. The slits sample the beam in two places and the resulting diffracted beams interfere with each other at the position of the detector.

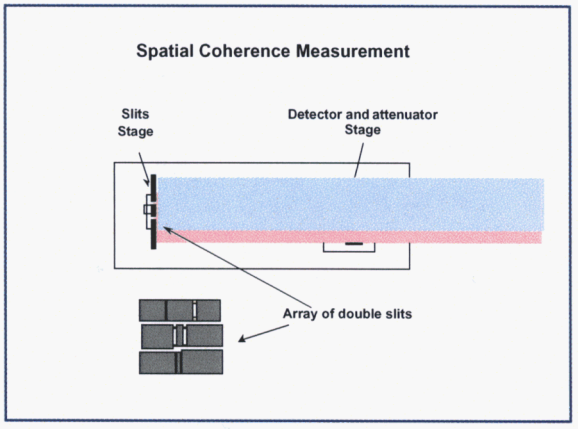

Figure 6.8 Spatial coherence measurement

At 0.8 keV the slits will be assembled from polished sticks of low-Z material such as B_4C or Si, held apart by spacers. The higher resolution "slits" for 8 keV will be manufactured by the sputter-sliced method or from an array of fibers.

6.8 Spatial Shape and Centroid location

The spatial shape and centroid location of the FEL beam will be measured on a pulse-by-pulse basis by the Scattering Foil Detectors located in the facility diagnostics tanks distributed along the beam lines.

6.9 Divergence

This measurement is performed at 8 keV using the Scattering Foil Detectors located along the beam line. The measurement is performed at 0.8 keV using the LCLS Segmented Ion Chambers located along the beam line.

Summary and conclusion

The Linac Coherent Light Source is the first in a new class of light sources. The unprecedented brightness implies a high energy loading on optics and diagnostics, and offers the opportunity for design innovations. Optics designs have been presented involving the use of a far-field experimental hall, a gas absorption cell, low-Z optics, and

grazing incidence optics. Part of the R&D strategy is to utilize an example of each type of optical design early in the experimental program, to gain experience. Should these be insufficient, optics whose surfaces can be continuously replenished have been considered (e.g. liquids and plasmas). There is also the solution of dynamic solid state optics, that are spatially translated between shots. Concerning diagnostics, we have given examples of the research and development being pursued. While a simple design strategy has been presented to deal with the extraordinary fluences, it is clear that further experimental and theoretical work is required.

Acknowledgements

Work performed under the auspices of the U.S. Department of Energy by Lawrence Livermore National Laboratory under contract No. W-7405-ENG-48.

References

1. Report of the Basic Energy Sciences Advisory Committee, Panel on Novel Coherent Light Sources, January 1999, available at: http://www.er.doe.gov/production/bes/BESAC/NCLS_rep.PDF.
2. J. B. Murphy and C. Pellegrini, "Introduction to the Physics of the Free Electron Laser," in *Frontiers of Particle Beams*, M. Month, S. Turner, eds., Lecture Notes in Physics **No. 296**, H. Araki et al, eds., Springer-Verlag, Berlin, pp. 163-212 (1988).
3. M. Cornacchia et al., "Performance and design concepts of a free-electron laser operating in the x-ray region," *SPIE Proceedings* **2988**, p2, (1997).
4. J. Arthur et al., *LCLS Design Study Report*, Internal Stanford University report SLAC-R-521, Rev. December 1998 UC-414 (1998).
5. *LCLS, The First Experiments*, available at: http://www-ssrl.slac.stanford.edu/lcls/papers/LCLS_experiments_2.pdf.
6. R. Tatchyn , J. Arthur, R. Boyce, T. Cremer, A. Fasso, J. Montgomery, V. Vylet, D. Walz, R. Yotam , A. K. Freund, M. R. Howells "X-ray Optics Design Studies for the 1.5-15 Å Linac Coherent Light Source (LCLS) at the Stanford Linear Accelerator Center (SLAC)", Paper Presented at the 1997 SPIE Annual Meeting, August 1, 1997, San Diego, CA; ms. #3154-22; *SPIE Proc.* **3154**; pp. 174-222 (1998).
7. R. Tatchyn, "LCLS Optics: Technological Issues and Scientific Opportunities," in *Proceedings of the Workshop on Scientific Applications of Short Wavelength Coherent Light Sources*, SLAC Report 414; SLAC-PUB 6064, March 1993
8. R. A. London, R. Bionta, R. Tatchyn and S. Roessler "Computational Simulations of High Intensity X-Ray Matter Interaction" in Proc SPIE, Optics for Fourth Generation X-ray Sources, **Vol 4500** p51, ed. R. Tatchyn, A. Freund and T. Matsushita, (2001) (2001)
9. Wootton, A. J., Arthur, A., Barbee, T., Bionta, R., London, R., Park, H-S., Ryutov, D., Spiller E., and Tatchyn, R "X-ray optics and diagnostics for the first experiments on the Linac Coherent Light Source", UCRL-JC-144183 (2001), and Proc SPIE, Optics for Fourth Generation X-ray Sources, **Vol 4500** p113, ed. R. Tatchyn, A. Freund and T. Matsushita, (2001), and A. Wootton, Arthur J., Barbee T., Bionta R., Jankowski A., London R., Ryutov D., Shepherd R., Shlyaptsev V., Tatchyn R., Toor A., Nuclear Instruments & Methods in Physics Research Section A-Accelerators Spectrometers Detectors & Associated Equipment. **483**, p345 (2002).
10. Jaroslav Kuba, Alan Wootton, Richard M. Bionta, Ronnie Shepherd, Ernst E. Fill, Todd Ditmire, Gilliss Dyer, James Dunn, Raymond F. Smith, Richard A. London, Vyacheslav N. Shlyaptsev, Sa_a Bajt, Michael D. Feit, Rick Levesque and Ronald H. Conant: "X-ray Optics Research for the

Linac Coherent Light Source: Interaction of ultra-short X-ray laser pulses with optical materials", 8th International Conference on X-Ray Lasers, Aspen, Colorado, USA, May 27 – 31 (2002)
11. Jaroslav Kuba, Alan Wootton, Richard M. Bionta, Ronnie Shepherd, Ernst E. Fill, Todd Ditmire, Gilliss Dyer, Richard A. London, Vyacheslav N. Shlyaptsev, James Dunn, Raymond F. Smith, Sa_a Bajt, Michael D. Feit, Rick Levesque and Mark McKernan: "X-ray Optics Research for Free Electron Lasers: Study of Material Damage Under Extreme Fluxes", 24th International Free Electron Laser Conference, Argonne National Laboratory, Chicago, Illinois, USA, Sept. 19-23 (2002)
12. B. C. Stuart et al., J. Opt. Soc. Am. B **13** p459 (1996)
13. D. D. Ryutov and A. Toor, "X-ray Attenuation cell". LCLS technical note 00-10, and LLNL internal report UCRL-ID-138125 (2000).
14. R. M. Bionta, "Controlling Dose to Low Z Solids at LCLS", LCLS note LCLS-TN-00-3
15. D. Gallagher and R. Hardesty, "Machining of Beryllium" in Metals Handbook **Vol 16** – Machining (ASM International, Metals Park, 1989) pp. 870-3
16. A. Jankowski, et al., "Nano-crystalline and hard boron-alloyed Be coatings", Mater. Res. Soc. Symp. Proc. Vol. **593** pp. 489-492 (2000)
17. D. D. Ryutov and A. Toor. "Optical elements based on the use of renewable liquid films with magneto-electrostatic control." Rev. Sci. Instr., **72**, p.4042, Nov. 2001, UCRL-JC-141538
18. Wootton, A J and D D. Ryutov "Diagnostics Imaging, weakly-perturbing diagnostics of an x-ray beam at the LCLS facility (physics issues)" LLNL report UCRL-ID-145967 (2002), accepted for publication in Rev. Sci. Instrum.
19. V. N. Shlyaptsev and A. Toor, "Plasma lens for high-flux radiation", in Proc SPIE, Optics for Fourth Generation X-ray Sources, **Vol 4500** p133, ed. R. Tatchyn, A. Freund and T. Matsushita, (2001)